Cement and Concrete Research 175 (2024) 107380

Contents lists available at ScienceDirect

Cement and Concrete Research

journal homepage: www.elsevier.com/locate/cemconres

Rheology and 3D printing of alginate bio-stabilized earth concrete

Yierfan Maierdan [a], Samuel J. Armistead [c], Rebecca A. Mikofsky [d], Qiqi Huang [b], Lola Ben-Alon [b], Wil V. Srubar III [c,d], Shiho Kawashima [a,*]

[a] Columbia University, Department of Civil Engineering and Engineering Mechanics, New York, NY 10027, USA
[b] Columbia University, Graduate School of Architecture, Planning and Preservation, New York, NY 10027, USA
[c] University of Colorado Boulder, Department of Civil, Environmental, and Architectural Engineering, USA
[d] University of Colorado Boulder, Materials Science and Engineering Program, USA

ARTICLE INFO

Keywords:
Kaolinite
Soil
Biopolymer
Microstructural analysis
Additive manufacturing

ABSTRACT

Driven by the need for sustainable construction solutions, there is renewed interest in earth-based materials. Biopolymer stabilizers can enhance the rheological and structural properties of these materials to facilitate their use in 3D printing. This research examined the influence of sodium alginate on the stability, particle interaction, rheology, and 3D printability of kaolinite, a commonly found clay in soils deemed suitable for construction. Findings revealed that sodium alginate could boost electrostatic interactions to enhance the stability of kaolinite suspensions. This rise in repulsive potential energy could reduce storage modulus and yield stress by orders of magnitude. However, as the alginate content increased beyond its critical overlapping concentration (0.12 %–0.6 %), a reverse trend was observed, which was attributed to the formation of a three-dimensional polymer network. Furthermore, alginate addition shifted the "printability window" of kaolinite mixtures to higher solid contents, which has positive implications on the strength and shrinkage of the printable mixtures.

1. Introduction

Earth construction has been in practice since 7000 BCE [1]; an estimated 30 % of the world's population resides in earthen buildings to this day [2]. In modern concrete, calcined clays have been used as supplementary cementitious materials (SCMs) to partially replace Portland cement to lower the associated carbon emissions. However, the substitution levels are usually limited to 20–30 % [3–5]. Recently, earth-based materials have been regaining popularity in the construction industry due to their environmental, economic, and health advantages [6–9]. From an environmental standpoint, raw clays and clay-rich soils offer a low carbon, minimally processed, and recyclable alternative to concrete [10], while achieving adequate strengths required for construction. Economically, earth construction can be highly affordable due to readily available materials from or around the construction site, such as the soils excavated for foundations [11,12]. From an indoor environmental quality (IEQ) and health point of view, earth assemblies were shown to act as passive removal materials for VOCs [13], while exhibiting excellent moisture buffering capacities, acting as a relative humidity "fly-wheel" that absorbs and desorbs moisture from and to the ambient air while maintaining optimal humidity levels for human comfort and thermal survivability [14,15].

The increasing focus on sustainable construction methods, coupled with advancements in digital fabrication, has led to increased attention to the potential of 3D-printed earth to bring about a transformative impact on low-carbon buildings. Notably, when considering carbon emissions from a life cycle assessment (LCA) perspective, it has been demonstrated that 3D-printed earth materials exhibit superior performance compared to 3D-printed concrete, surpassing it by 85 % overall [16]. This improvement translates into an 88 % enhancement in environmental sustainability concerning global warming impacts, as well as an 83 % reduction in land use requirements [16].

To date, however, the majority of 3D printed earth examples, such as the Gaia House and the Tecla Habitat [17,18], have primarily served as experimental and educational endeavors, showing a great need for further extensive scientific evaluation of the raw materials or the physical and chemical properties of the 3D printed paste. This absence of rigorous examination includes crucial aspects like fresh-state rheology and mechanical property characterization. Consequently, several obstacles hinder the widespread adoption of 3D-printed earth construction. These challenges include limited knowledge in manufacturing techniques, extended material drying durations, and an absence of

* Corresponding author.
E-mail address: s-kawashima@columbia.edu (S. Kawashima).

https://doi.org/10.1016/j.cemconres.2023.107380
Received 23 August 2023; Received in revised form 20 October 2023; Accepted 9 November 2023
Available online 14 November 2023
0008-8846/© 2023 Elsevier Ltd. All rights reserved.

consistent and reliable technical data regarding the workability and printability properties of materials, as well as the optimal ratios of water and additives.

Existing studies on the scientific and technological characterization of 3D printed earth include environmental evaluations and processing parameters. In a study on 3D-printed cob-like mixtures, an environmental LCA was conducted from cradle to site, showing that 3D-printed earth incurs 91 % less global warming impacts than 3D-printed concrete [16]. From a processing and mechanical performance perspective, the behavior of earthen mix designs for 3D printing was assessed to indicate possible extrusion rates through a printing nozzle, motion speed, and layer heights [19]. While the aforementioned research provides valuable insights, it primarily focused on the environmental impact and printing procedure of raw earth materials. This necessitates additional investigations to discern the specific cause-and-effect relationships within the microstructural interaction, rheology, and printing status.

The utilization of earth as a construction material necessitates the inclusion of supplementary additives and stabilizers due to inherent challenges: the material variability, sensitivity to the water [20], significant settling behavior, slow structural build-up, and low mechanical properties pose concerns that need to be addressed. Recent research from architecture, civil, and geotechnical engineering suggests that these challenges could be mitigated with the use of biopolymer additives, enhancing the mechanical and chemical properties of earth-based materials [21,22]. A prevalent biopolymer, sodium alginate, sourced from the cell walls of marine brown algae with an alginic acid content of 30–60 %, is frequently employed. Transforming alginic acid to sodium alginate enables it to dissolve in water, facilitating a liquid-gel behavior in aqueous solutions and transitioning from a low-viscosity state to a gel-like structure [23]. Notably, Perrot et al. [24] successfully confirmed the practicability of 3D printing with sodium alginate-stabilized earth, observing a quicker structural development compared to pure earth mixtures—an essential trait for reducing processing time during 3D printing. However, there is currently a limited understanding of the interaction between clay and sodium alginate, particularly the mechanisms by which these entities interact and influence each other. The nature of this interplay is significant as it profoundly influences the fresh state rheology of the mixture. Furthermore, these rheological traits, derived from polymer-clay interaction, can provide crucial insights to govern the 3D printing process. This understanding can also contribute to the predictive models that inform the final printing status. Therefore, bridging this knowledge gap is fundamental to unlocking new potentials in the use of biopolymers in earth-based additive manufacturing.

The primary objectives of this research are to investigate the interaction between kaolinite clay and sodium alginate biopolymer and examine its impact on the fresh state rheology and 3D printability of kaolinite-alginate suspensions, with a specific emphasis on elucidating the potential use of sodium alginate for 3D printable earth concrete. The investigative journey begins with an examination of how sodium alginate impacts the stability of kaolinite suspensions, followed by a detailed exploration of the microstructural characteristics that underlie this stabilization mechanism. Subsequently, the rheological performance of kaolinite-alginate mixtures with different clay/water ratios and different alginate additions was studied. This investigation enables the elucidation of the intricate network of particle interactions and their consequential effects on the rheological properties of these mixtures. Furthermore, the effect of clay/water ratio and alginate addition on 3D printability was examined, establishing a connection with the rheological characteristics. Through these investigations, valuable insights were obtained into the complex interplay between particle interactions, rheology, and printing outcomes that contribute to the fundamental understanding required to advance biopolymer-facilitated additive manufacturing.

2. Theory: interaction forces in a suspended system

Understanding the dominant interaction forces within suspended systems is crucial for comprehending the structure-property-function relationship of materials. These interactions play a pivotal role in determining the stability, homogeneity, and rheological behavior of suspensions under various conditions. In a suspended system, interaction forces can be classified into three categories: colloidal interaction, Brownian force, and viscous interaction [25,26]. Among them, Brownian force originates from the random movement of suspended particles due to the thermal energy of the solvent molecules (i.e., suspended particles being subject to random bombardment by solvent molecules.) [27,28]. If the suspended particles are small enough ($\ll 1$ μm [29]) to be significantly affected by these stochastic collisions from solvent molecules, the suspension could be defined as a Brownian suspension. In contrast, with an increase in particle size, the Brownian force becomes negligible, and thereby, the Brownian force can be neglected. In addition, the classification between Brownian and non-Brownian suspensions is also affected by flow conditions. The competition between the Brownian thermal diffusion and advection rate caused by flow is characterized by the Péclet number (Eq. (1)). When the Péclet number $Pe \gg 1$, the advection effect dominates, and the suspension could be seen as non-Brownian [27,29]. Regarding the significant large particle size (around 1 to 67 μm) of the clay used in this study, kaolinite suspensions could be considered as non-Brownian suspensions.

$$Pe = \frac{Advection\ rate}{Diffusion\ rate} = \frac{\eta_s \dot{\gamma} a^3}{k_B T} \tag{1}$$

where, $\dot{\gamma}$ indicates shear rate; η_s is the viscosity of the solvent; k_B represents Boltzmann constant; T indicates absolute temperature; and a is the particle radius.

Colloidal interactions arise from particle-particle interactions, which include London-van der Waals, electrostatic, steric, and depletion interactions [30]. London-van der Waals attraction forces include three distinct types: dipole-dipole interaction, dipole-induced dipole interaction, and London dispersion force. Of these, the London dispersion force (as depicted in Fig. 1a) stands out as the most crucial. This force arises from transient electrostatic interactions originating from the temporary polarization of electron distributions within atoms or molecules. London-van der Waal forces are significant when the distance between two particles is small enough (around 5 nm or less) [25,29]. For two equal-sized spherical particles, the potential energy of van der Waals forces could be given by the Hamaker expression (Eq. (2)) [31]. In a suspended system, the van der Waals attraction forces between suspended particles should be decreased (van der Waals forces decrease with the increase in inter-particle distance) during colloidal processing to obtain desirable stability and homogeneity. This can be accomplished by increasing interparticle repulsion forces, such as steric, electrostatic, and depletion interactions, thereby raising the potential energy barrier to van der Waals attractions. [30].

$$U_{vdW} = -\frac{A}{6}\left(\frac{2}{s^2-4} + \frac{2}{S^2} + ln\frac{s^2-4}{s^2}\right) \tag{2}$$

where, $s = \frac{2a+h}{a}$, a indicates the particle radius, and h indicates the minimum separation between the two particles' surface.

Steric interactions (Fig. 1b), also known as steric repulsion forces, originate from the surface coating of polymers or nonionic surfactants. When two coated particles approach each other, the absorbed polymer chains overlap, and the repulsive forces arise from the following three reasons: i) the concentration of polymer in the overlapping zone increases significantly, resulting in an increase in the osmotic pressure, therefore creating osmotic repulsive force between the particles; ii) the coated polymer layer works as a physical barrier between particles; iii) another source for the repulsive force comes from the decrease in the

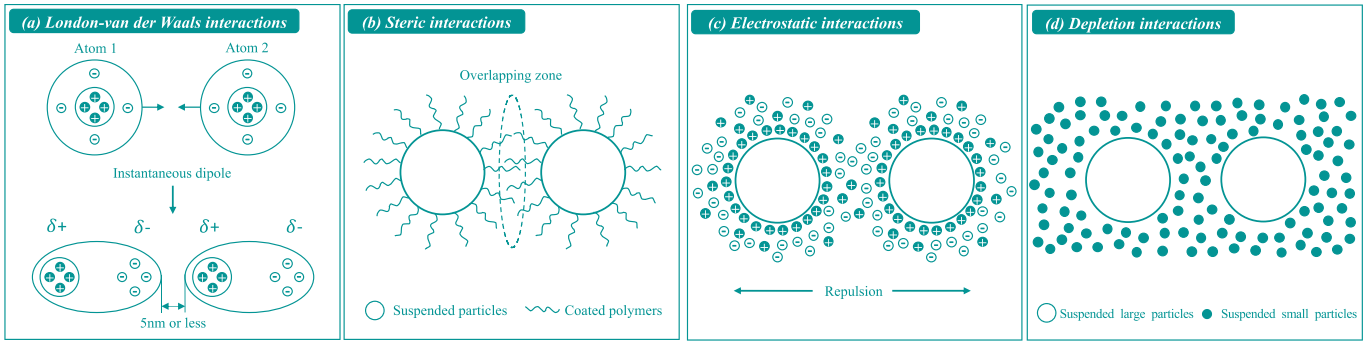

Fig. 1. Colloidal interactions: (a) London-van der Waals interactions; (b) steric interactions; (c) electrostatic interactions (d) depletion interactions.

configurational entropy of the polymer chain due to decrease in the volume availability in the overlapping zone [25]. Additionally, electrostatic repulsive forces (Fig. 1c) emerge either from the presence of surface charges on the particle or from the existence of absorbed ionic surfactants. The phenomenon of depletion interaction (Fig. 1d) occurs when larger colloidal particles are suspended within a suspension of smaller nonabsorbing particles. Depletion interaction may accelerate flocculation or stabilization of the suspension depending on the depletant size. Overall, the stability of suspensions at rest is governed by total interparticle potential energy, U_{total}, which could be expressed by Eq. (3) [30]. In cases where interparticle interactions result in a net repulsion, it signifies that the particles remain separated, leading to a stable suspension. Conversely, if the interparticle interactions yield a net attractive force, the particles tend to agglomerate and flocculate.

$$U_{total} = U_{vdW} + U_{elect} + U_{steric} + U_{dep} \quad (3)$$

In the equation, U_{vdW} represents the attractive potential arising from van der Waals forces, while U_{elect} and U_{steric} correspond to the repulsive energies resulting from electrostatic and steric interactions, respectively. Additionally, U_{dep} signifies the potential energy associated with depletion interactions.

Whilst colloidal interactions indicate particle-particle interactions, in contrast, viscous interaction (i.e., hydrodynamic interaction) denotes the interactions between the matrix and suspended particles, which originates from the friction between suspended particles and the solvent [32]. Overall, both colloidal and viscous interactions must be taken into account when analyzing the rheological behavior of suspensions under flow conditions [30,33,34].

3. Materials and methods

3.1. Raw materials

The water used in this study was distilled or MiliQ ultrapure water. Sodium alginate (Sigma-Aldrich) had a pH of 6 at a 1 % concentration in water at 25 °C. Kaolinite clay (Sigma-Aldrich) was used as-received for rheological, 3D printing, zeta potential, and settling column tests. Kaolinite clay used for mineral binding characterization (thermogravimetric analysis (TGA), Fourier transform infrared spectroscopy (FTIR)) and particle size analysis was heated in an oven at 100 °C for 5 h to remove free water, ground with a mortar and pestle, and sieved to ensure a particle size <45 μm (Gilson SS-3 with No. 325, No.200, and No. 120 sieves).

Microstructural images of the kaolinite particles were captured using a Zeiss Sigma VP Scanning Electron Microscope (SEM). As illustrated in Fig. 2, the kaolinite particles exhibited a characteristic plate-like structure. X-ray Fluorescence was used to confirm the chemical composition of kaolinite (SiO_2 and Al_2O_3 account for 58.88 % and 33.07 %, respectively) (see Table 1). The particle size distribution of the kaolinite was determined using a Malvern Panalytical Mastersizer 3000, which revealed a range of approximately 1 to 67 μm and a median particle size of 8.7 μm.

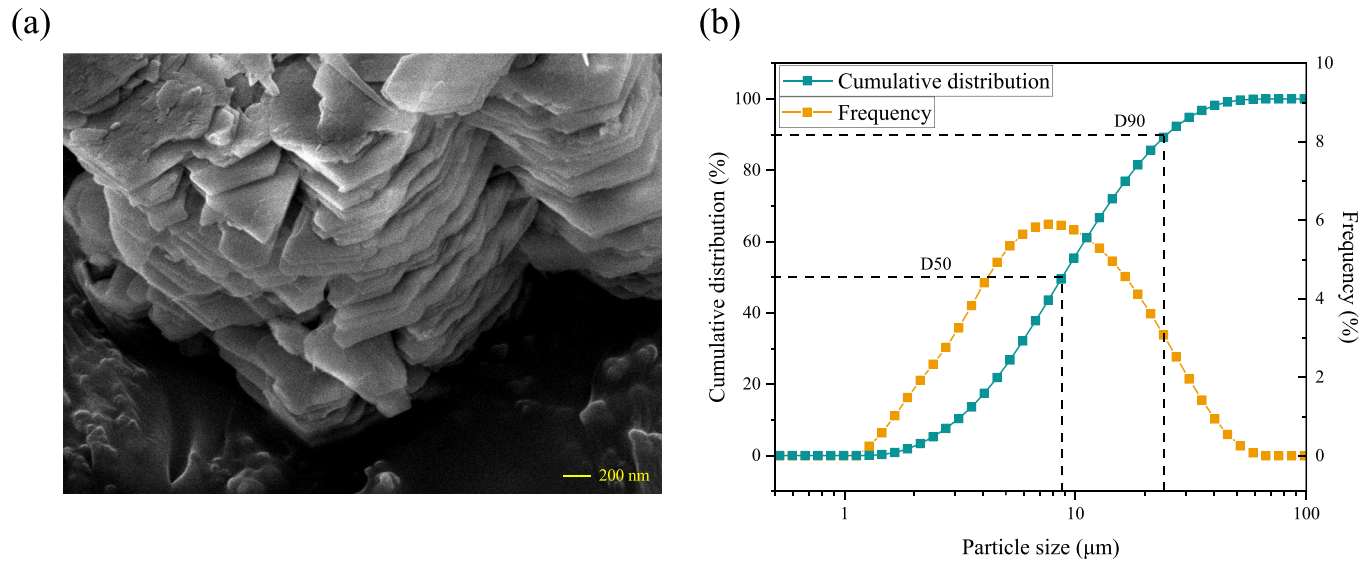

Fig. 2. Material characterizations: (a) SEM image and (b) particle size distribution of the kaolinite powder used in this research.

Table 1
Chemical composition of kaolinite clay.

Chemical composition	Percentage (%)
SiO_2	58.88
Al_2O_3	33.07
K_2O	3.70
Fe_2O_3	1.39
TiO_2	0.88
PbO	0.79
BaO	0.60
SO_3	0.41
CuO	0.09

3.2. Mixture proportions

For kaolinite suspensions, the Mix IDs were designated as KxWx, where K and W represent the masses of kaolinite and water in grams, respectively. For example, a mixture with ID K60W50 denotes the use of 60 g of kaolinite powder and 50 g of water. In the case of kaolinite-alginate suspensions, Mix IDs were established as KxWx_Ax, where A indicates the proportion of alginate relative to the mass of water. For instance, a kaolinite-alginate suspension with ID K60W50_A2.4 corresponds to a mixture of 60 g of kaolinite, 50 g of water, and 1.2 g (i.e., 2.4 % of 50 g) of sodium alginate. It should be noted that the addition of these three materials is independent of each other. When investigating the effect of the clay/water ratio, only the clay content was increased while the water and alginate content remained unchanged. Similarly, when studying the impact of different alginate content, only the alginate content was modified while the clay and water content remained constant.

3.3. Mixing procedure

To prepare the samples for the rheology test and 3D printing test, the materials were first weighed and then placed in separate containers. For the creation of kaolinite-alginate suspensions, the desired content of alginate (i.e., 0.06, 0.12, 0.6, 1.2, or 2.4 %) was dissolved in distilled water with the aid of mixing by hand and with a hand mixer (Hamilton Beach, Model: 62637). The hand mixer was consistently set at its highest speed throughout sample preparation. Next, the kaolinite (according to the mix design, from 40 to 120 g) was added to the alginate solution, mixed for 1 min with a hand mixer, stirred with a spoon for 1 min to prevent it from sticking to the container, then followed by an additional minute of mixing with a hand mixer to ensure thorough blending. The mixture was then added into a sandblasted cylindrical cup for rheology testing or a syringe for 3D printing. Before testing, the mixture was placed on a vibrating table for 1 min to eliminate air bubbles. The entire process, from adding the kaolinite to the alginate solution (or distilled water for pure kaolinite suspensions) until the start of the tests (rheology or 3D printing), took 7 min for all mixtures.

3.4. Rheological tests

The rheological properties of the samples were assessed using a TA DHR 20 Rheometer equipped with a vane geometry and a sandblasted cylindrical cup at a temperature of 25 °C. Prior to each test, a pre-shear of 220 s^{-1} [35] was applied for 300 s to remove the shear history, followed by a 30-s rest period. An oscillation strain amplitude sweep (with strain ranging from 10^{-3} % to 10^{3} %, constant frequency 1 Hz [36]) was used to determine the critical strain (i.e., the extent of the linear viscoelastic range (LVR)) and corresponding storage modulus, which characterizes the material's ability to store and release elastic energy when subjected to applied stress. The evolution of storage modulus was evaluated by applying a constant oscillating strain within the LVR (0.005 % for all mixtures) for 1 h. Furthermore, the static yield stress, representing the minimum stress threshold for flow initiation, and the dynamic yield stress, denoting the stress magnitude required to maintain flow under dynamic conditions, were determined using a constant shear rate of 1 s^{-1}. Rheological tests were performed a minimum of three times for each sample, and the resulting average values are reported.

3.5. Settling column tests

In order to assess the impact of sodium alginate on the stability of kaolinite suspensions, a series of settling column tests were performed using 100 mL graduated cylinders. Each suspension was prepared by adding 10 g of kaolinite to 100 mL of distilled water and varying quantities of sodium alginate (0 %, 0.06 %, 0.12 %, 0.6 %, 1.2 %, and 2.4 % relative to the mass of water). Subsequently, 100 mL of each suspension was poured into the graduated cylinders, and the clay-water interface was recorded within 1 h.

3.6. Microstructural analysis

3.6.1. Mineral binding characterization sample preparation

Kaolinite-alginate samples were synthesized to assess clay-biopolymer binding through the methodology described by Armistead et al. [21,37]. First, sodium alginate powder was slowly added to 40 °C water with constant stirring to achieve 0.01 M based on polymer subunits and incubated at 40–50 °C for 10 min, then removed from heat and sonicated for 10 min. Once the solution was cooled down, 50 mg of kaolinite was added to 20 mL of 0.01 M sodium alginate solution and sonicated for an additional 10 min, and mixed with a LabNet Mini LabRoller for 30 min. To remove the unbound biopolymer from the clay, the mixture was centrifuged at 4000 rpm for 10 min, the supernatant was disposed of, and then 20 mL of water was added. This washing procedure was repeated for a total of 5 centrifuges (including initial supernatant removal). Then the sample was dried under ambient conditions and ground for analysis.

3.6.2. Mineral binding characterization analysis

Microscale characterization included TGA (TA instruments Discovery 5500), and FTIR (ThermoScience iS20). TGA was performed from room temperature to 800 °C heated at 5 °C/min. FTIR spectrograms were measured using a Ge-ATR accessory at a resolution of 4 cm^{-1} from 600 to 4000 cm^{-1} with 64 scans.

3.7. Zeta potential

Zeta potential measurements were performed using a Malvern Zetasizer Nano-ZS. The samples were prepared using the same method as the rheology samples. 0.1 wt% kaolinite was suspended in solutions containing 0 %, 0.06 %, and 0.12 % alginate (in a 10 mM NaCl solution) to assess the effect of alginate on the zeta potential. To ensure statistically significant results, each data point was derived from five different samples, with each sample tested three times, resulting in an average of 15 measurements per data point.

3.8. 3D printing tests

In order to assess the 3D-printability of the mixtures, cylindrical samples were printed using a syringe gantry printer equipped with a 60 mL syringe and a 2.4 mm diameter circular nozzle. The samples had a height and outer diameter of 25.4 mm. The printing speed was maintained at 40 mm/s, and additional details about the 3D printer can be found in reference [38]. Printing of the mixtures began 7 min after initial contact between the kaolinite and alginate solution (or distilled water for kaolinite suspensions). The printed samples were subsequently classified into one of three categories: "Too flowable," "Printable," or "Unprintable".

4. Results and discussions

4.1. Settling column tests

Results of the settling experiments are shown in Fig. 3. The settling experiments were conducted on both the kaolinite suspension and kaolinite-alginate suspensions with varying alginate content. The experiments had a duration of 1 h, which was chosen to correspond with the fresh state rheology and 3D printing experiments. The purpose of the settling experiments was to examine the effect of sodium alginate on the stability and sedimentation behavior of the kaolinite suspension. Data in Fig. 3 revealed that the kaolinite suspension significantly settled due to the flocculation and agglomeration of clay particles under van der Waals forces [39], reaching approximately 50 % settling after 1 h. Similar results were also observed by Shakeel et al. [40]. However, the addition of sodium alginate showed a noticeable reduction in the settling behavior of the kaolinite suspension. For example, with 0.06 % sodium alginate, settling decreased from around 50 % to 10 %. Further increasing the alginate content led to a decrease in settling to <2 % within the one-hour experiment. These results indicate that the addition of sodium alginate enhances the stability of the kaolinite suspension in the fresh state (note: kaolinite-alginate suspensions will also settle after a few hours) and reduces the attraction potential energy caused by particle interaction (or may change the net attractive U_{total} to net repulsion). The subsequent section aims to determine which component of the repulsive interactions was responsible for the increased stability and the energy barrier against the van der Waals attractive forces.

4.2. Microstructural analysis

Zeta potential measurements were conducted to investigate the electrostatic interaction between kaolinite and alginate. As depicted in Fig. 4a, the zeta potential of the kaolinite suspension was approximately −39 mV. However, after adding sodium alginate to the kaolinite suspension, the zeta potential exhibited a statistically significant decrease to approximately −50 mV. This observation indicates that the addition of sodium alginate increased the electrostatic repulsion energy (U_{elect}) between the particles. Fig. 4b and c displays the TGA-DTG and FTIR results of the analyzed samples. The red line corresponds to the washed kaolinite sample derived from the kaolinite suspension, while the blue line represents the washed kaolinite from the kaolinite-alginate suspensions. The washing process was repeated four times to eliminate unbound polymers. TGA results did not show a noticeable difference in mass loss between pure kaolinite and the kaolinite-alginate suspensions (the mass loss change within the error margin). Likewise, FTIR analysis revealed little difference between pure kaolinite and kaolinite-alginate suspensions. Comparing these results to the findings reported by Mikofsky et al. [22] with the same washing process for kaolinite but with different biopolymers, the variations in mass loss and changes in FTIR peaks were much more pronounced with the non-ionic biopolymers (e.g., guar gum) than with sodium alginate. Changes in FTIR peaks and TGA mass loss difference correspond to chemical interactions (i.e., binding) between kaolinite and different biopolymers. The absence of changes to the FTIR spectra and TGA in this study is likely due to the electrostatic repulsion between kaolinite and alginate, both of which carry negative charges, hindering their binding and surface absorption.

In summary, the analysis of physicochemical interactions between kaolinite and sodium alginate demonstrates that sodium alginate heightens the energy barrier for van der Waals attraction forces through an increase in the electrostatic repulsion energy of kaolinite particles. More specifically, the zeta potential experiments provide compelling evidence that the addition of alginate significantly enhances the electrostatic repulsion forces within the kaolinite suspension. Mineral binding characterization, including TGA and FTIR experiments, further indicated that significant chemical interactions between kaolinite and sodium alginate do not exist. Thus, the findings collectively indicate that electrostatic repulsion predominantly governs the stabilization of kaolinite in solution with sodium alginate, with depletion interaction possibly playing a role.

4.3. Rheological properties

4.3.1. Critical strain and linear viscoelasticity

In order to identify the LVR and analyze the strain dependency of the mixtures, strain amplitude sweeps were conducted. The critical strain is the final value of the LVR, detected when the storage modulus experiences a perceptible decline from the plateau value. Typically, the acceptable range of deviation falls within 5–10 % (ISO 6721-10 and DIN 51810-2). This study defined the critical strain as a 10 % decrease from the plateau value. Based on the results presented in Fig. 5, two main findings can be drawn.

Firstly, the critical strain was found to decrease with an increase in the kaolinite/water ratio (Fig. 5c). In the case of kaolinite suspensions, for example, the critical strain decreased from 0.042 % to 0.012 % when the kaolinite/water ratio increased from 40/50 to 70/50. This trend was more pronounced in kaolinite-alginate suspensions, where the critical strain decreased significantly from 1.4 % to 0.06 % as the kaolinite/water ratio increased from 40/50 to 70/50. The decrease in critical strain can be linked to enhanced particle interactions. A general model for particle distance could be introduced at this point. The average distance between particles, referred to as '*h*,' can be calculated using the Woodcock model, as outlined in Eq. (4) [29]. Importantly, even though

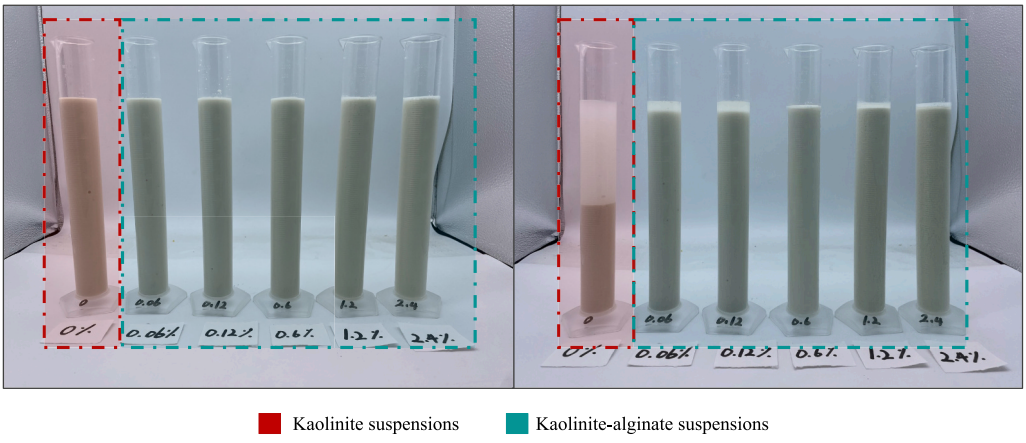

Fig. 3. Settling column tests: (a) starting status of settling experiments (b) after 1 h of settling.

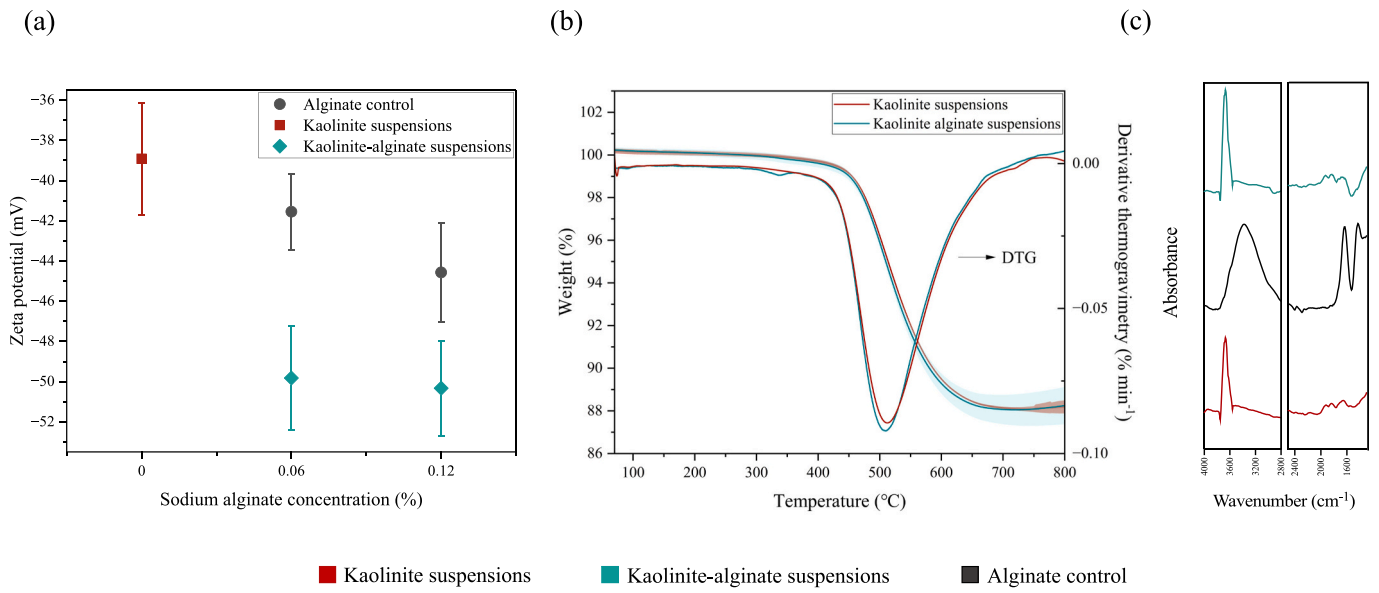

Fig. 4. Microstructural analysis: (a) zeta potential; (b) thermogravimetric analysis results; (c) FTIR results of kaolinite suspension, alginate control, and kaolinite-alginate suspensions.

the clay used in this study featured a plate-like structure rather than a spherical one, the fundamental inverse correlation between volume fraction and particle distance remains consistent. This implies that as the concentration of kaolinite increases, the distance between particles decreases, resulting in greater particle interactions, as reflected in the notably higher modulus (Fig. 5e) [41]. However, this also increases the risk of breaking the particle interaction network since the network could function as a transfer path for force. Consequently, even minor deformations can be transmitted through the interaction paths, causing particle rearrangement and, ultimately, the breakdown of the linearity [42].

$$\frac{h}{d} = \left[\left(\frac{1}{3\pi\varnothing} + \frac{5}{6}\right)^{0.5} - 1\right] \tag{4}$$

where h is the average distance between particles, $\varnothing$ indicates phase volume, and d is the diameter of the particle.

Secondly, as shown in Fig. 5c and d, the inclusion of sodium alginate considerably extended the LVR and a critical alginate content of 0.12 % was identified to achieve the highest critical strain. Initially, the critical strain exhibited an increasing trend as the alginate content was raised from 0 % to 0.12 %, peaking at the 0.12 % addition. However, in the range of 0.12 % to 2.4 %, the critical strain decreased with increasing alginate content. Nevertheless, even at the highest sodium alginate concentrations, the critical strain remained significantly higher than that of the pure kaolinite suspension. For instance, the critical strain for k60w50_A2.4 was 0.207 %, markedly surpassing the value of 0.013 % for k60w50. In the case of kaolinite suspensions, particle flocculation naturally occurs, leading to the formation of a three-dimensional network structure due to van der Waals forces [39]. The flocculation structure of a kaolinite suspension taken by cryo-scanning electron microscopy (cryo-SEM) could be found in the reference [43], which was simplified as Fig. 6a. Consequently, the applied deformation can easily propagate through the particle network, resulting in a lower critical strain. However, as shown in Fig. 6b, when a small amount of sodium alginate (0– 0.12 %) was present in kaolinite suspensions, the electrostatic stabilization inhibited particle flocculation, thereby impeding the formation of the particle network. Under this condition, the mixture exhibited the highest strain independency. As the sodium alginate concentration (C) continues to increase, it reaches a critical concentration (C*) where polymer overlapping occurs [25]. Beyond this threshold, the polymers start to overlap with each other, forming a three-dimensional polymer network (Fig. 6c). This explains the decrease in critical strain and the increase in the plateau value once the polymer content surpasses 0.12 %. It is important to mention that this critical concentration may be different from pure polymer solutions' critical overlapping concentration (a commonly used concept in soft matter science) because there is a competition between polymer overlapping and electrostatic stabilization. The plateau value begins to rise, and the critical strain commences its descent when polymer overlapping gains the upper hand in this competition.

4.3.2. *Yield stresses*

To determine the static and dynamic yield stresses, the samples were subjected to a constant shear rate of 1 s^{-1}. The shear stress responses of the mixtures are plotted in Fig. 7a and b. The static yield stress was identified as the highest value observed within the first 30 s, while the dynamic yield stress was calculated as the average value during the last 30 s. The specific values of static and dynamic yield stress are presented in Fig. 7c and d. The difference between the static and dynamic yield stresses allows for the characterization of structural decomposition, an important parameter of thixotropy, which can be defined as the ratio between the static yield stress and the dynamic yield stress [44].

The influence of the kaolinite/water ratio on the yield stress of the mixtures is illustrated in Fig. 7a and c. As expected, both the static and dynamic yield stress of the mixture increased with higher kaolinite content, attributable to enhanced particle interactions. The results depicted in Fig. 7b and d illustrate that the addition of sodium alginate significantly reduced both the dynamic and static yield stress of the mixtures. As elucidated in the preceding section, the presence of sodium alginate effectively prevents the flocculation and agglomeration of kaolinite particles through its stabilization mechanism. Therefore, in the case of kaolinite suspensions, clay aggregates could have a significantly higher resistance to shear due to the large geometric size and stronger particle interaction network. On the other hand, in the kaolinite-alginate suspensions, the particles remain separate, resulting in lower yield stress.

However, as the alginate content is further increased from 0.12 % to 2.4 %, the alginate concentration reaches its critical concentration C* [25]. This phenomenon causes the formation of three-dimensional polymer networks, which consequently increase the flow resistance and yield stress. Nevertheless, strain amplitude sweep tests revealed that

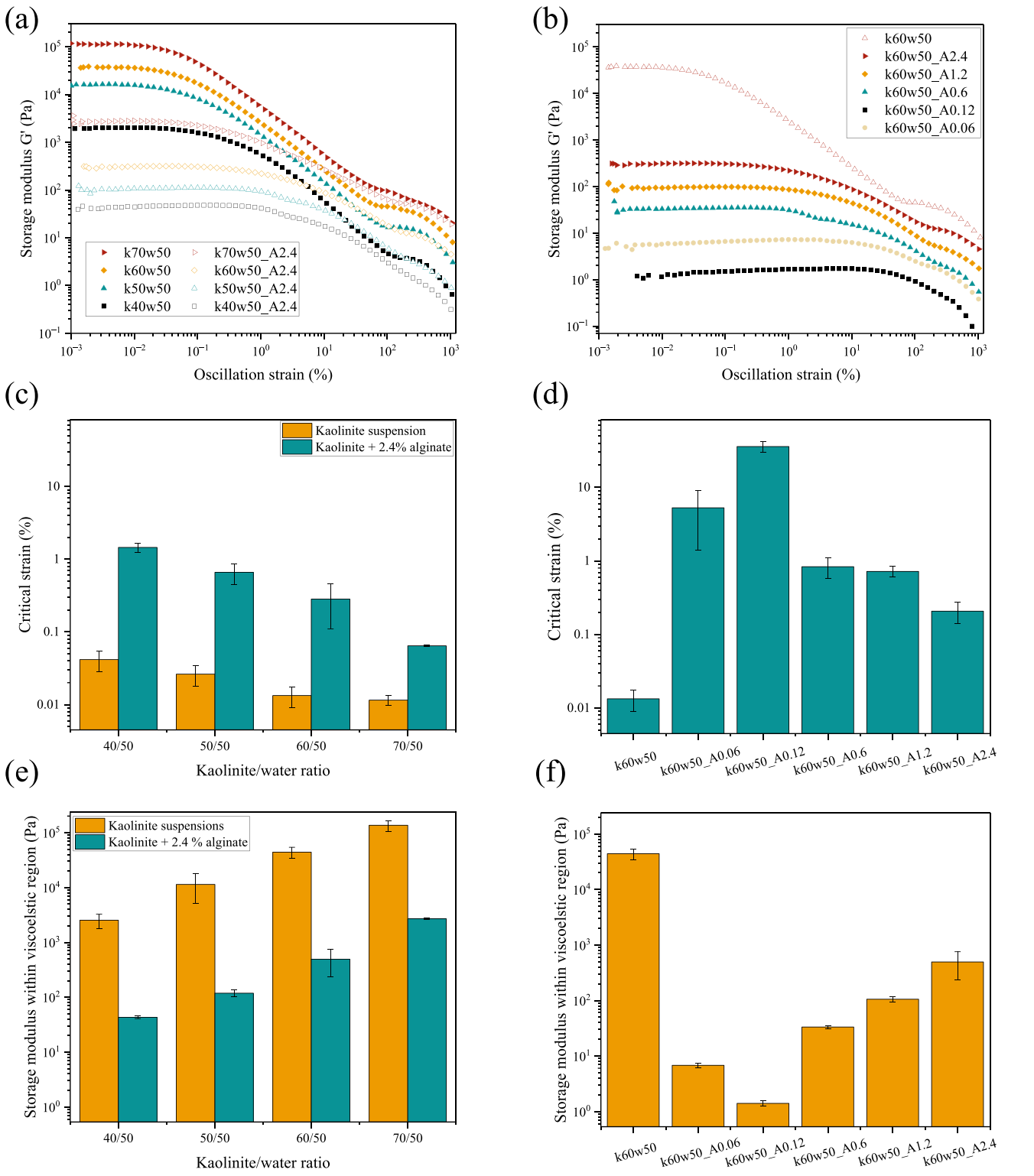

Fig. 5. Oscillation strain amplitude sweep: (a) effect of kaolinite/water ratio and (b) different sodium alginate content on the viscoelasticity; (c) effect of kaolinite/water ratio and (d) different sodium alginate content on the critical strain (e) effect of kaolinite/water ratio and (f) different sodium alginate content on the storage modulus within the linear viscoelastic region.

the kaolinite-alginate suspensions exhibit enhanced deformability compared to kaolinite suspension. This can be attributed to the elongated and folded characteristics of the polymer chains. Therefore, the over-lapped kaolinite-alginate suspensions could deform along the flow direction, subsequently, exhibiting a lower flow resistance compared to the pure kaolinite suspensions. Consequently, the overlapped clay-polymer mixture (alginate content: 0.12–2.4 %) presents higher yield stress compared to the without overlapped clay-polymer mixture (alginate content: 0–0.12 %), but lower yield stress than pure clay suspensions.

Notably, the reduction in static yield stress caused by sodium alginate was more pronounced compared to the dynamic yield stress. Unlike

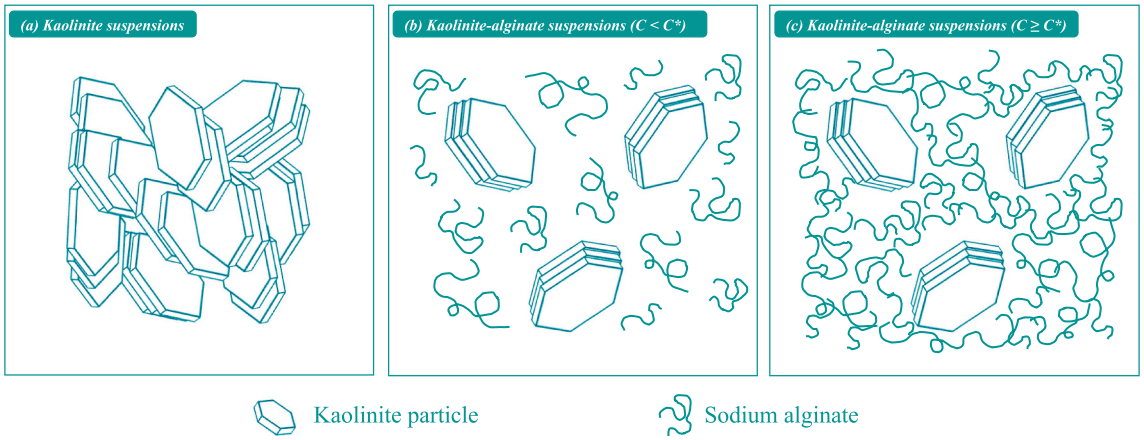

Fig. 6. (a) The three-dimensional network created by the natural flocculation of kaolinite particles; (b) the stabilization mechanism of alginate before reaching its critical overlapping concentration (C*); (c) the three-dimensional network created by alginate after reaching the critical overlapping concentration.

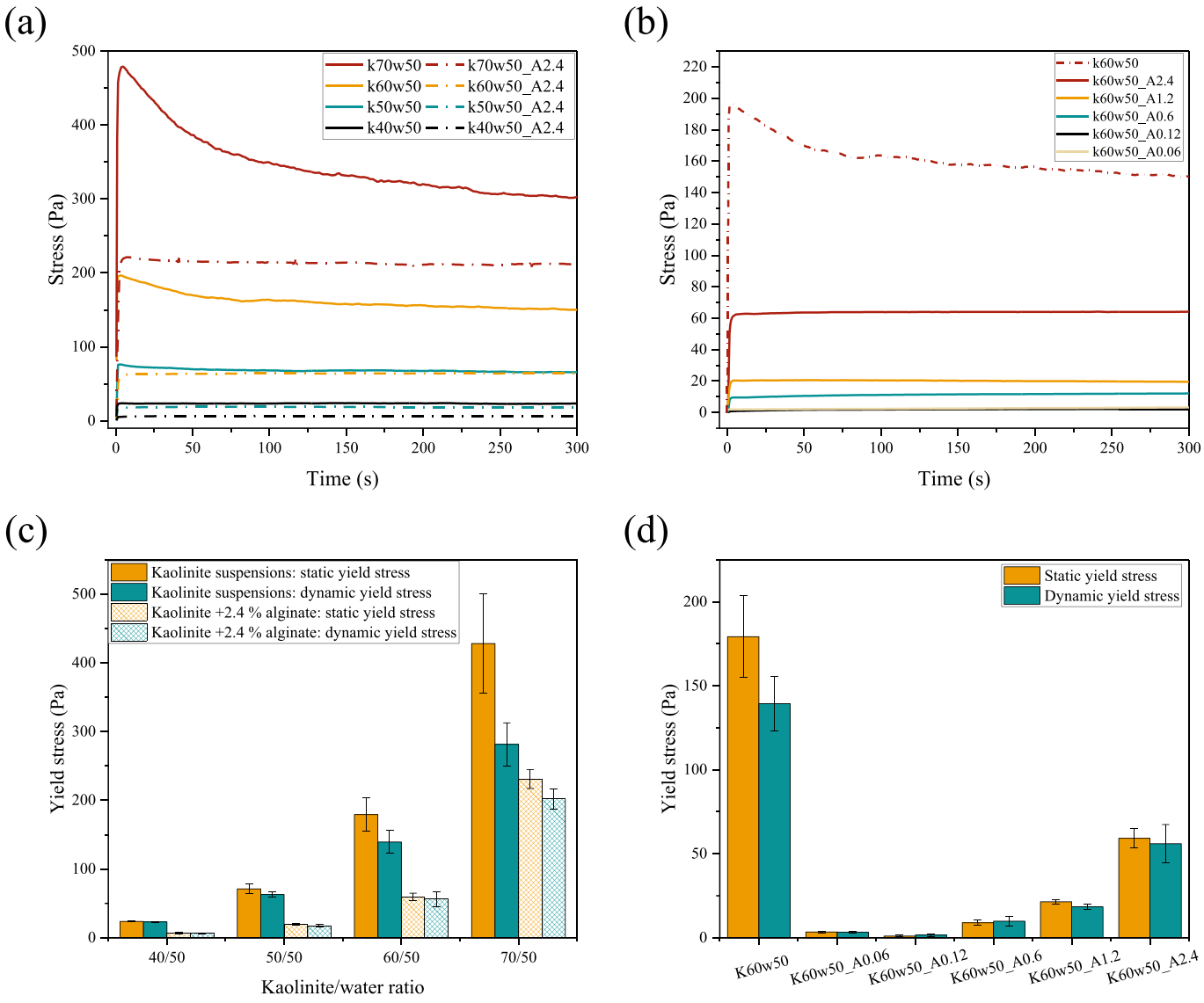

Fig. 7. Static yield stress: (a) effect of kaolinite/water ratio and (b) alginate content on the shear stress response; (c) effect of kaolinite/water ratio and (d) alginate content on the static and dynamic yield stress.

kaolinite suspensions, the inclusion of sodium alginate resulted in the absence of a significant peak in static yield stress, indicating a substantially lower level of thixotropy. In kaolinite suspensions, the applied constant shear broke down the kaolinite flocs into smaller aggregates, thereby reducing flow resistance compared to the flow onset. A significant decrease in shear stress response was observed, characterized by a distinct peak in static yield stress, especially at higher kaolinite/water ratios. However, the strong deformability and separated structure of the kaolinite-alginate suspensions prevented a substantial decrease in shear stress response, enabling easy alignment with the flow direction, and presented significantly lower thixotropy.

4.3.3. Storage modulus evolution

Fig. 8 presents the storage modulus evolution obtained by applying oscillation shear strain within the LVR (0.005 %) for 1 h. Fig. 8a shows the effect of the kaolinite/water ratio on the storage modulus evolution. Similar to the oscillation strain amplitude sweep, the storage modulus of kaolinite suspensions and kaolinite-alginate suspensions increased with clay/water ratios due to the rise in the solid content and the more intense particle interactions. To assess the rate of structural recovery, a linear model was constructed using data collected between 1000 s and 3600 s, with the slope serving as the evaluation criterion. A similar method was also applied by other researchers to measure the structural recovery rate of mixtures [45]. Table.2 provides the values of parameter k for kaolinite suspensions and kaolinite-alginate suspensions, exhibiting an increase corresponding to the clay content. The rise in clay content results in a decrease in particle-particle distance and an increase in the number of surrounding particles around each clay particle. Consequently, a greater number of particle interactions are formed simultaneously, leading to an accelerated rate of structural recovery (see Fig. 9). Fig. 8b illustrates the impact of sodium alginate content on the time-dependent behavior of the storage modulus. Consistent with the findings from LVR and yield stress analyses, the storage modulus initially decreased and then increased with increasing sodium alginate content. Similarly to Fig. 8a, mixtures with higher initial storage modulus exhibited a faster rate of structural recovery in Fig. 8b.

Table 2
The calculated structural recovery rate.

Mix ID	Slope (k)
Effect of clay/water ratio	
k40w50	0.33
k50w50	0.68
k60w50	1.24
k70w50	2.06
k40w50_A2.4	0.004
k50w50_A2.4	0.008
k60w50_A2.4	0.034
k70w50_A2.4	0.16
Effect of sodium alginate content	
k60w50	1.12
k60w50_A0.06	0.0144
k60w50_A0.12	0.0025
k60w50_A0.6	0.0064
k60w50_A1.2	0.016
k60w50_A2.4	0.034

4.4. Printability evaluation

The printability of the mixtures was assessed through the fabrication of 25.4 mm cylindrical samples. In this evaluation, two crucial parameters were considered: extrudability, signifying the material's capacity to extrude smoothly and continuously from the nozzle, and buildability, indicating the mixtures' ability to maintain their shape due to adequate yield stress. Based on these two parameters, the printed mixtures were categorized into three distinct groups. Mixtures displaying substantial yielding behavior were classified as "Too Flowable" due to insufficient buildability. "Printable" denoted mixtures that exhibited smooth, uninterrupted surfaces without yielding behavior, signifying favorable buildability and printability. On the other hand, "Unprintable" was used for mixtures that demonstrated significant surface cracks during extrusion, known as the "sharkskin effect," indicating unfavorable extrudability.

Fig. 10 illustrates the printability assessment of the mixtures, where the kaolinite/water ratio gradually increases from left to right. The results demonstrate the existence of a distinct "printability window." As depicted in Fig. 10, as the kaolinite/water ratio rises, the mixture exhibits a more solid-like behavior, causing a transition in printing quality from "Too flowable" to "Printable." These findings align with the rheology test results, which presented an increase in yield stress with a rise in kaolinite/water ratios. For printed structure, the stress theoretically induced by gravity typically falls within the range of ρgH to $\rho gH/\sqrt{3}$ [46]. The yield stress obtained from Section 4.3.2 was used to predict the mixture's printability, which is presented in Fig. 11. Within this

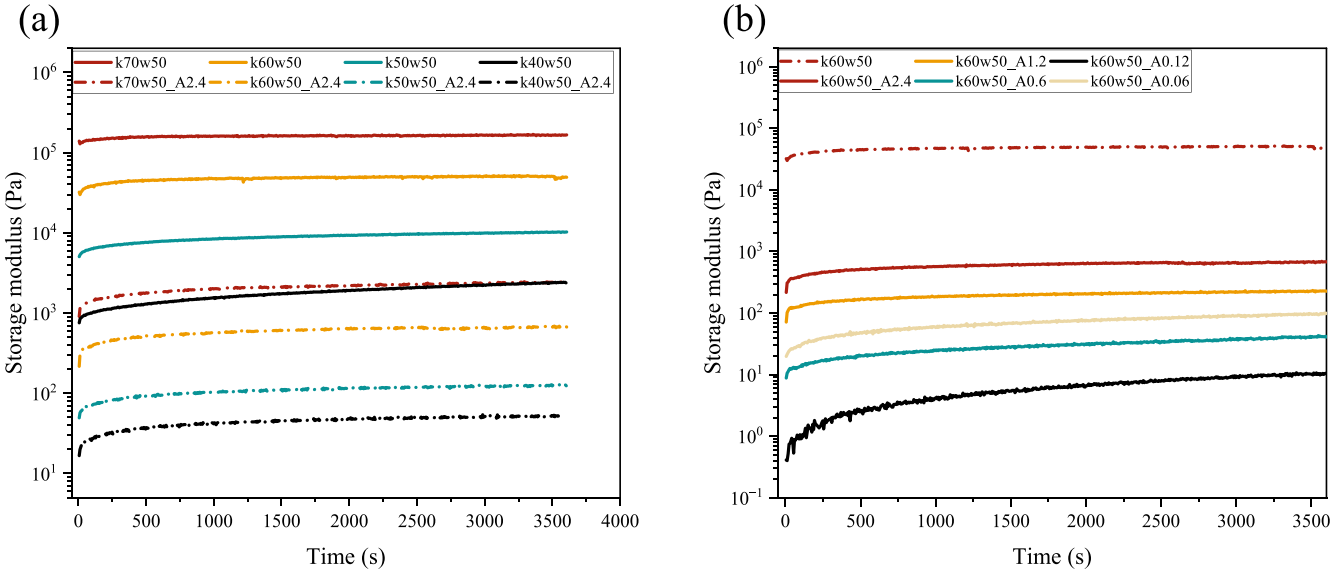

Fig. 8. Oscillation time sweep: (a)effect of kaolinite/water ratio; (b) effect of different sodium alginate content on the time evolution of the mixtures.

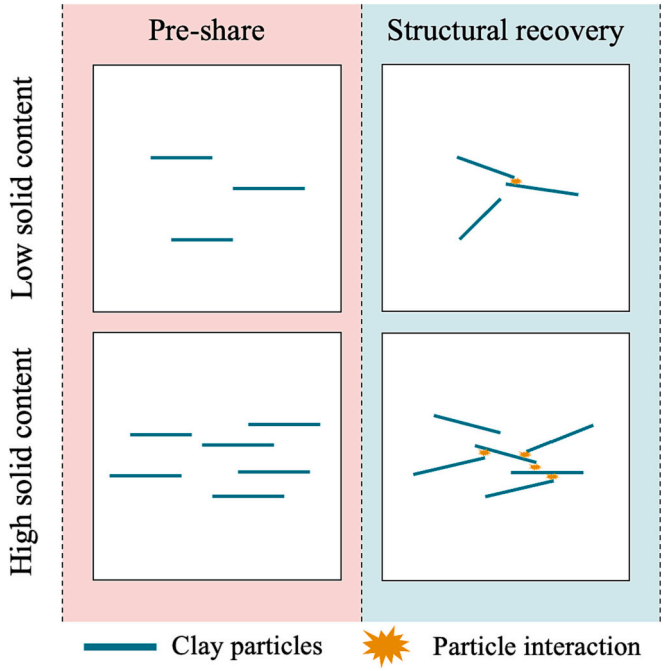

Fig. 9. Influence of solid content on structural recovery rate under horizontal flow conditions (idealized particle alignment for clarity).

figure, the red area symbolizes the stress theoretically induced by gravity. As shown in Fig. 11, the transition point from "Too flowable" to "Printable" could be defined as the point at which the mixture's yield stress exceeds the stress due to gravity. It is important to mention that the main purpose of this section is to understand the effect of kaolinite/water ratio and alginate addition on the general trend of printing performance. It should importantly be noted that the suspensions experience different shear histories between the applied shear protocol to measure yield stress and printing. Still, the measured yield stress gave an accurate prediction of the printing status (All the data gave correct predictions. Therefore, inaccurate predictions did not appear in the figures). As the kaolinite/water ratio continues to increase, the kaolinite suspension begins to exhibit the sharkskin effect and becomes prone to cracking during the printing process, thereby transitioning from "Printable" to "Unprintable."

Fig. 10 shows a specific printability window for kaolinite suspensions, with different kaolinite/water ratios ranging from 70/50 to 85/50. The addition of 2.4 % alginate significantly decreased the mixtures' yield stress. As a result, the printability window for the kaolinite-alginate suspensions was shifted to a higher kaolinite/water ratio (from 85/50 to 110/50). Therefore, the addition of sodium alginate enabled the smooth and continuous printing of the mixture with a high clay/water ratio. This characteristic has considerable potential to increase the mechanical strength of the final printable mixture (same for castable mixtures) and decrease drying shrinkage.

4.5. *Significance*

Converging lines of evidence suggest that sodium alginate has a superplasticizing effect on clay suspensions. Specifically, the inclusion of sodium alginate significantly increased the fresh-state flowability, indicated by decreases in yield stress (two orders of magnitude) and storage modulus (four orders of magnitude). These changes in rheology were similarly evident in the results of 3D printing experiments, where the sodium alginate addition shifted the printability "window" to higher

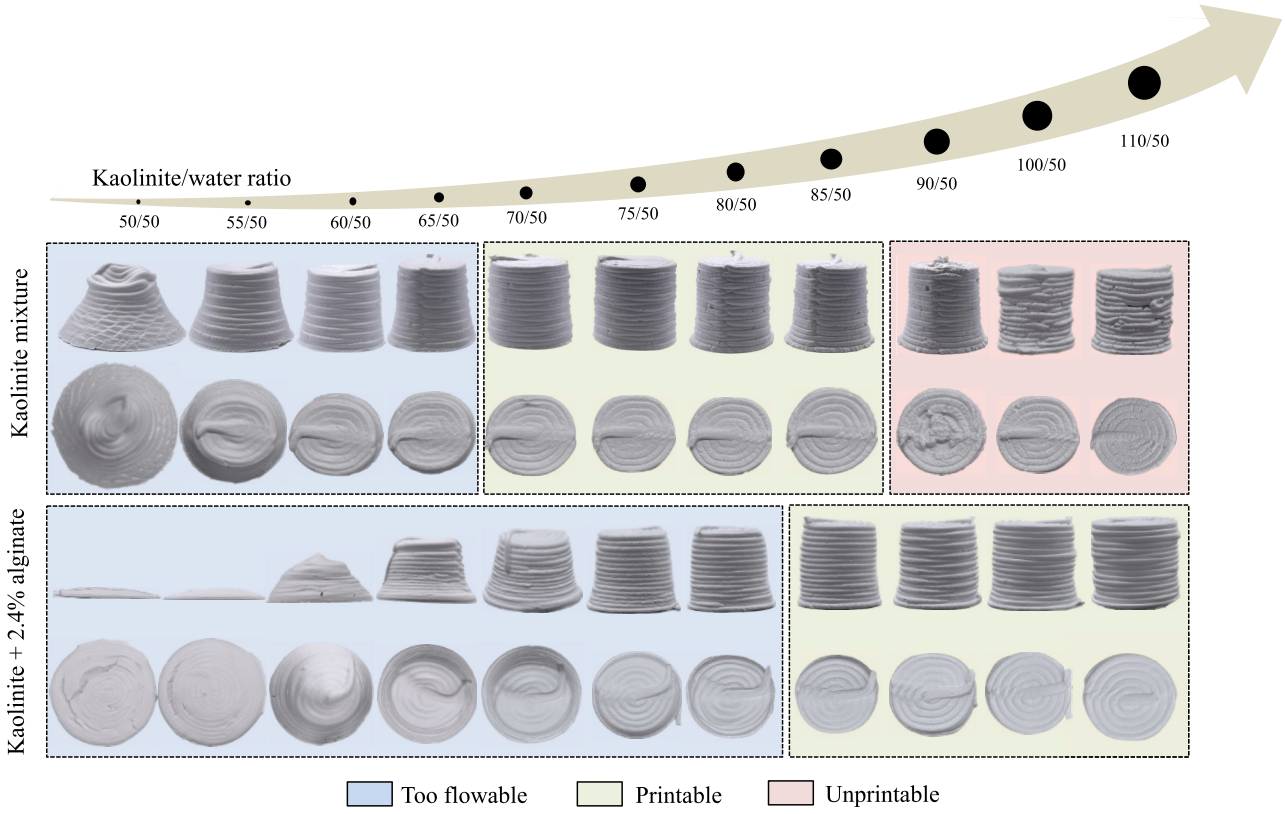

Fig. 10. Effect of kaolinite/water ratio and sodium alginate addition on the printing behavior of mixtures. Kaolinite/water ratio increase from left to right. For the kaolinite mixture, the print status gradually changes from "Too flowable" to "Printable" and then "Unprintable." With the addition of sodium alginate, the printability window of samples shifted to higher kaolinite/water ratios.

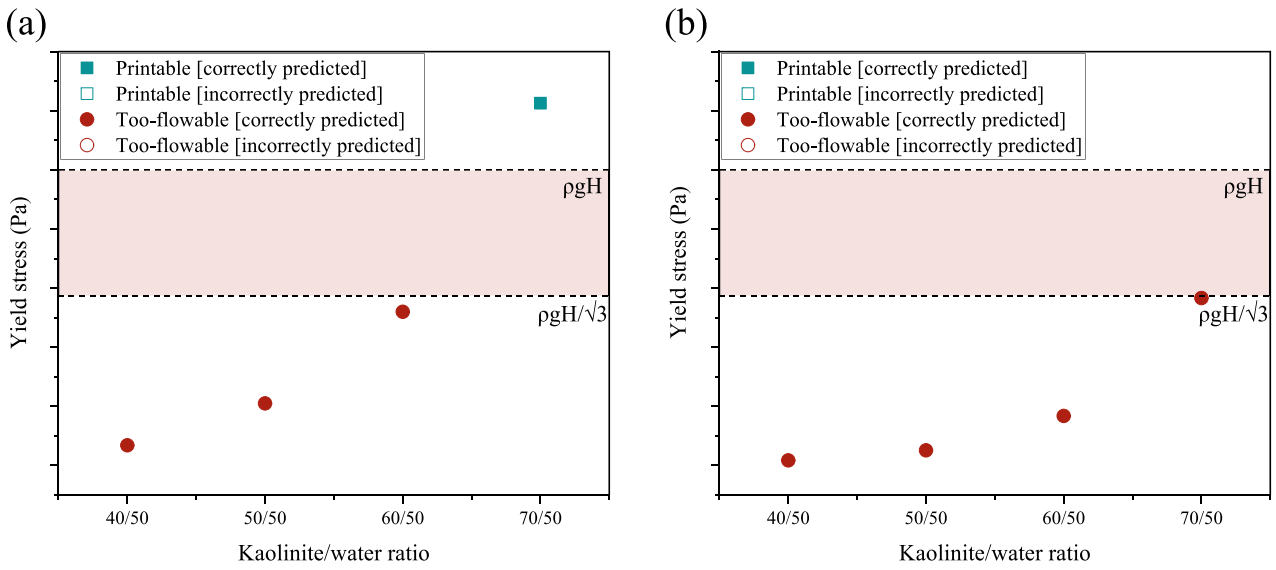

Fig. 11. The prediction of printing status by the yield stress obtained from 1 s^{-1} constant shear: (a) kaolinite suspensions; (b) kaolinite +2.4 % alginate.

clay/water ratios. Combining the findings from previous research on the alginate-stabilized earth-based materials [24], we can conclude that sodium alginate can accelerate the structural build-up of earth-based materials but also work as a superplasticizer. Therefore, sodium alginate has the potential to serve as an effective thixotropic admixture to decrease water demand while still achieving sufficient printability, which has positive implications for increasing final strength and decreasing drying shrinkage of 3D-printed earth concrete.

5. Conclusions

This study explored the sedimentation behavior, particle interactions, rheology, and 3D printability of kaolinite-alginate mixtures. The primary aim of the investigation was to establish a connection between fundamental microscale particle interactions and the macroscale flow behavior and viscoelastic properties. Then, the distinctive rheological characteristics were used to predict the printing status of the final structure. Based on the results, the following conclusions have been drawn:

- Settling column tests revealed that the kaolinite suspension naturally flocculates and settles due to van der Waals forces. However, the addition of sodium alginate reduced sedimentation behavior and increased fresh-state stability.
- Microstructural analysis revealed that sodium alginate negatively increased the zeta potential of kaolinite suspensions (from −39 mV to around −50 mV). Mineral binding characterization further indicated the absence of significant chemical interactions between kaolinite and sodium alginate. Therefore, the primary stabilization mechanism of sodium alginate to kaolinite is electrostatic stabilization.
- The structuration of particles leads to an enhanced storage modulus and diminished critical strain. Specifically, the storage modulus increases with the clay/water ratio but decreases with the addition of the polymer. On the other hand, the critical strain decreases as the clay/water ratio increases but increases with the addition of the polymer. The yield stress exhibits a similar trend to the storage modulus, increasing with structuration and decreasing with stabilization.
- Sodium alginate has a critical concentration somewhere between 0.12 % and 0.6 %. Beyond this concentration, the sodium alginate started to overlap with each other to create a three-dimensional polymer network, consequently, increasing the storage modulus and the yield stress of kaolinite-alginate suspensions.
- The printability evaluation revealed a specific printability window for kaolinite suspensions, with different kaolinite-to-water ratios ranging from 70/50 to 85/50. The addition of sodium alginate shifted the printability window to higher kaolinite/water ratios (from 85/50 to 110/50), enabling the continuous and smooth extrusion of mixtures with higher solid content. This development holds promising prospects for bolstering the final strength and mitigating drying shrinkage in 3D-printed earth concrete.

For future research, exploring the mechanical properties and durability (e.g., water resistance) of kaolinite-alginate composites would be a pertinent direction. Additionally, conducting a comparative study to assess the superplasticizing effect of sodium alginate in earth-based materials in contrast to traditional concrete superplasticizers would provide valuable insights into the potential applications of sodium alginate in construction and material science. For mitigating the material variability, the clay used in this study was exclusively focused on kaolinite clay. As such, a limitation of this research is its singular focus on the interaction between kaolinite and sodium alginate, which may not be universally applicable to other clay minerals. Expanding the scope to include various clay minerals and long-term durability assessments would offer more comprehensive insights into alginate bio-stabilized earth concrete.

CRediT authorship contribution statement

Yierfan Maierdan: Conceptualization, Methodology, Data curation, Visualization, Validation, Formal analysis, Investigation, Writing – review & editing, Writing – original draft. **Samuel J. Armistead:** Methodology, Investigation, Visualization, Formal analysis, Writing – review & editing. **Rebecca A. Mikofsky:** Methodology, Formal analysis, Validation, Investigation, Writing – review & editing. **Qiqi Huang:** Investigation, Visualization. **Lola Ben-Alon:** Conceptualization, Writing – review & editing, Project administration, Funding acquisition. **Wil V. Srubar:** Writing – review & editing, Project administration, Funding acquisition. **Shiho Kawashima:** Conceptualization, Methodology, Writing – review & editing, Project administration, Funding acquisition.

Declaration of competing interest

The authors declare the following financial interests/personal

relationships which may be considered as potential competing interests: Shiho Kawashima reports financial support was provided by the National Science Foundation.

Data availability

Data will be made available on request.

Acknowledgments

The authors would like to acknowledge the National Science Foundation for financial support (Award #2134488), and technical support provided by the staff of Carleton Laboratory at Columbia University.

References

[1] F. Pacheco-Torgal, S. Jalali, Earth construction: lessons from the past for future eco-efficient construction, Constr. Build. Mater. 29 (2012) 512–519, https://doi.org/10.1016/j.conbuildmat.2011.10.054.
[2] L. Miccoli, U. Müller, P. Fontana, Mechanical behaviour of earthen materials: a comparison between earth block masonry, rammed earth and cob, Constr. Build. Mater. 61 (2014) 327–339.
[3] R. Snellings, P. Suraneni, J. Skibsted, Future and emerging supplementary cementitious materials, Cem. Concr. Res. 171 (2023), 107199.
[4] D. Zhao, R. Khoshnazar, Microstructure of cement paste incorporating high volume of low-grade metakaolin, Cem. Concr. Compos. 106 (2020), https://doi.org/10.1016/j.cemconcomp.2019.103453.
[5] D. Zhao, R. Khoshnazar, Hydration and microstructural development of calcined clay cement paste in the presence of calcium-silicate-hydrate (C–S–H) seed, Cem. Concr. Compos. 122 (2021), https://doi.org/10.1016/j.cemconcomp.2021.104162.
[6] Y. Maierdan, K. Gu, B. Chen, M.A. Haque, Y. Zhang, L. Zhao, Recycling of heavy metal contaminated river sludge into unfired green bricks: strength, water resistance, and heavy metals leaching behavior – a laboratory simulation study, J. Clean. Prod. 342 (2022), 130882, https://doi.org/10.1016/j.jclepro.2022.130882.
[7] Y. Maierdan, M.A. Haque, B. Chen, M. Maimaitiyiming, M.R. Ahmad, Recycling of waste river sludge into unfired green bricks stabilized by a combination of phosphogypsum, slag, and cement, Constr. Build. Mater. 260 (2020), 120666, https://doi.org/10.1016/j.conbuildmat.2020.120666.
[8] Y. Maierdan, Q. Cui, B. Chen, M. Aminul Haque, A. Yiming, Effect of varying water content and extreme weather conditions on the mechanical performance of sludge bricks solidified/stabilized by hemihydrate phosphogypsum, slag, and cement, Constr. Build. Mater. 310 (2021), 125286, https://doi.org/10.1016/j.conbuildmat.2021.125286.
[9] D. Ardant, C. Brumaud, A. Perrot, G. Habert, Robust clay binder for earth-based concrete, Cem. Concr. Res. 172 (2023), 107207, https://doi.org/10.1016/j.cemconres.2023.107207.
[10] L. Ben-Alon, V. Loftness, K.A. Harries, G. DiPietro, E.C. Hameen, Cradle to site life cycle assessment (LCA) of natural vs conventional building materials: a case study on cob earthen material, Build. Environ. 160 (2019), 106150, https://doi.org/10.1016/j.buildenv.2019.05.028.
[11] M.C. Hardin, S. Merry, W. Fritz, Towards an affordable rammed-earth dwelling, in: Proceedings, 2003 PLEA (Passive Low Energy Archit. Conf.), 2003.
[12] L. Schroder, V. Ogletree, Adobe Homes for All Climates: Simple, Affordable, and Earthquake-resistant Natural Building Techniques, Chelsea Green Publishing, 2010.
[13] E.K. Darling, C.J. Cros, P. Wargocki, J. Kolarik, G.C. Morrison, R.L. Corsi, Impacts of a clay plaster on indoor air quality assessed using chemical and sensory measurements, Build. Environ. 57 (2012) 370–376.
[14] L. Ben-alon, A.R. Rempel, Thermal comfort and passive survivability in earthen buildings, Build. Environ. 238 (2023), 110339, https://doi.org/10.1016/j.buildenv.2023.110339.
[15] G. Minke, Building With Earth: Design and Technology of a Sustainable Architecture, De Gruyter, 2009.
[16] H. Alhumayani, M. Gomaa, V. Soebarto, W. Jabi, Environmental assessment of large-scale 3D printing in construction: a comparative study between cob and concrete, J. Clean. Prod. 270 (2020), 122463, https://doi.org/10.1016/j.jclepro.2020.122463.
[17] M. Marani, The Gaia House is a 3D-printed Prototype Made of Biodegradable Materials, Archit. Newsp, 2019.
[18] 3D WASP, 3D Printed House TECLA: Eco-housing. https://www.3dwasp.com/en/3d-printed-house-tecla/, 2019. (Accessed 13 July 2023).
[19] M. Gomaa, W. Jabi, A. Veliz Reyes, V. Soebarto, 3D printing system for earth-based construction: case study of cob, Autom. Constr. 124 (2021), 103577, https://doi.org/10.1016/j.autcon.2021.103577.
[20] A.E. Losini, A.C. Grillet, M. Bellotto, M. Woloszyn, G. Dotelli, Natural additives and biopolymers for raw earth construction stabilization – a review, Constr. Build. Mater. 304 (2021), 124507, https://doi.org/10.1016/j.conbuildmat.2021.124507.
[21] S.J. Armistead, C.C. Smith, S.S. Staniland, Sustainable biopolymer soil stabilisation: the effect of microscale chemical characteristics on macroscale mechanical properties, Acta Geotech. 0 (2022), https://doi.org/10.1007/s11440-022-01732-0.
[22] R.A. Mikofsky, S.J. Armistead, W.V. Srubar, On the Bonding Characteristics of Clays and Biopolymers for Sustainable Earthen Construction, Springer Nature, Switzerland, 2023, https://doi.org/10.1007/978-3-031-33465-8_22.
[23] L.A.L. dos Santos, Natural Polymeric Biomaterials: Processing and Properties, 2017.
[24] A. Perrot, D. Rangeard, E. Courteille, 3D printing of earth-based materials: processing aspects, Constr. Build. Mater. 172 (2018) 670–676, https://doi.org/10.1016/j.conbuildmat.2018.04.017.
[25] T.F. Tadros, Rheology of Dispersions: Principles and Applications, John Wiley & Sons, 2011.
[26] H.A. Barnes, J.F. Hutton, K. Walters, An Introduction to Rheology, Elsevier, 1989.
[27] N.J. Wagner, J. Mewis, Theory and Applications of Colloidal Suspension Rheology, Cambridge University Press, 2021.
[28] F. Chinesta, G. Ausias, Rheology of Non-spherical Particle Suspensions, Elsevier, 2015.
[29] M.M. Rueda, M.C. Auscher, R. Fulchiron, T. Périé, G. Martin, P. Sonntag, P. Cassagnau, Rheology and applications of highly filled polymers: a review of current understanding, Prog. Polym. Sci. 66 (2017) 22–53, https://doi.org/10.1016/j.progpolymsci.2016.12.007.
[30] J.A. Lewis, Colloidal processing of ceramics, J. Am. Ceram. Soc. 83 (2000) 2341–2359.
[31] H.C. Hamaker, The London—van der Waals attraction between spherical particles, Physica 4 (1937) 1058–1072.
[32] R.G. Larson, The Structure and Rheology of Complex Fluids, 1999.
[33] D.M. Bigg, Rheological behavior of highly filled polymer melts, Polym. Eng. Sci. 23 (1983) 206–210.
[34] H. Ohshima, Effective viscosity of a concentrated suspension of uncharged spherical soft particles, Langmuir 26 (2010) 6287–6294, https://doi.org/10.1021/la904121p.
[35] D. Zhao, J.M. Williams, A.H.A. Park, S. Kawashima, Rheology of cement pastes with calcium carbonate polymorphs, Cem. Concr. Res. 172 (2023), 107214, https://doi.org/10.1016/j.cemconres.2023.107214.
[36] T. Mezger, The rheology handbook: for users of rotational and oscillatory rheometers, in: European Coatings, 5th edition, 2020.
[37] S.J. Armistead, A.E. Rawlings, C.C. Smith, S.S. Staniland, Biopolymer stabilization/solidification of soils: a rapid, Micro-macro, cross-disciplinary approach, Environ. Sci. Technol. 54 (2020) 13963–13972, https://doi.org/10.1021/acs.est.0c02001.
[38] A.E. Douba, P. Badjatya, S. Kawashima, Enhancing carbonation and strength of MgO cement through 3D printing, Constr. Build. Mater. 328 (2022), 126867, https://doi.org/10.1016/j.conbuildmat.2022.126867.
[39] H.A. Barnes, A review of the rheology of filled viscoelastic systems, Rheol. Rev. 2003 (2003) 1–36.
[40] A. Shakeel, A. Kirichek, C. Chassagne, Rheology and yielding transitions in mixed kaolinite/bentonite suspensions, Appl. Clay Sci. 211 (2021), 106206, https://doi.org/10.1016/j.clay.2021.106206.
[41] A. Patti, D. Acierno, H. Lecocq, A. Serghei, P. Cassagnau, Viscoelastic behaviour of highly filled polypropylene with solid and liquid tin microparticles: influence of the stearic acid additive, Rheol. Acta 60 (2021) 661–673, https://doi.org/10.1007/s00397-021-01297-x.
[42] M.M. Rueda, R. Fulchiron, G. Martin, P. Cassagnau, Linear and non-linear nature of the flow of polypropylene filled with ferrite particles: from low to concentrated composites, Rheol. Acta 56 (2017) 635–648, https://doi.org/10.1007/s00397-017-1025-0.
[43] M.S. Zbik, R.S.C. Smart, G.E. Morris, Kaolinite flocculation structure, J. Colloid Interface Sci. 328 (2008) 73–80, https://doi.org/10.1016/j.jcis.2008.08.063.
[44] Y. Qian, K. Lesage, K. El Cheikh, G. De Schutter, Effect of polycarboxylate ether superplasticizer (PCE) on dynamic yield stress, thixotropy and flocculation state of fresh cement pastes in consideration of the Critical Micelle Concentration (CMC), Cem. Concr. Res. 107 (2018) 75–84, https://doi.org/10.1016/j.cemconres.2018.02.019.
[45] M.S. Nasser, A.E. James, Degree of flocculation and viscoelastic behaviour of kaolinite-sodium chloride dispersions, Colloids Surf. A Physicochem. Eng. Asp. 315 (2008) 165–175, https://doi.org/10.1016/j.colsurfa.2007.07.030.
[46] N. Roussel, Rheological requirements for printable concretes, Cem. Concr. Res. 112 (2018) 76–85, https://doi.org/10.1016/j.cemconres.2018.04.005.